PHYSICAL REVIEW E, VOLUME 64, 046405

Physical model of anode glow patterns in elevated-pressure gas discharges

R. Sh. Islamov
Institute of Laser and Information Technologies, RAS, 140700 Shatura, Moscow Region, Russia

(Received 30 April 2001; published 25 September 2001)

A physical self-consistent model is developed to explain single spots or complex current structures at the anode of elevated-pressure parallel-plate dc discharges. The model is based on a fluid description of electron and ion transport coupled with Poisson's equation and involves a pair of coupled reaction-diffusion equations of an activator-inhibitor-type. This system of one-dimensional equations containing no phenomenological (adjustable) parameters allows one to find the current-density (activator) and anode potential drop (inhibitor) distributions on the anode surface. In a certain range of supply voltage, an anode glow stratification, resulting in the formation of separate glowing regions, takes place. However, the growth of perturbations and formation of a spatially periodic current pattern are complicated by competition between the current stripes, leading to suppressing of the neighboring current stripes. The bifurcation behavior of the model with respect to the characteristic electron energy, recombination coefficient, and discharge gap has been analyzed. The properties of a single anode current structure, including the normal current density effect, have been investigated. The application of these results to available findings in experiments and two-dimensional numerical simulations is discussed.

DOI: 10.1103/PhysRevE.64.046405 PACS number(s): 52.80.Hc, 47.54.+r, 42.60.Lh

I. INTRODUCTION

The investigation of discharge stability and conditions for homogeneous discharge burning is of practical significance in a number of applications. It is known [1] that an elevated-pressure self-sustained glow discharge far from the walls of chamber is unstable with respect to constriction to the column at high current density. The anode spots are usually circular. The laminar gas flow transverse to the current destroys the column and the anode spots are converted into a number of stripes along the gas flow [1–4]. In the absence of gas flows stripe patterns in current distributions are observed in silent gas discharges [5] and dc discharge systems with a high-resistance semiconductor cathode [6]. The most credible cause of the plasma inhomogeneity formation near electrode is the negativity of a volt-ampere characteristic of the electrode layer [7], which is in conformity with the contraction dynamic and the weak sensitivity of instability evolution to discharge conditions and gas composition. Numerically within the frame of pure electrodynamic phenomena, the possibility of an instability growth in electrode regions has been shown in [8]. The spontaneous stratification of the glow in elevated-pressure gases has been demonstrated by numerical simulations in near-anode plasmas [4], dielectric barrier discharges [9], and discharges with metallic electrodes [10,11]. However, as in the case of physical experiments, the results of numerical experiments need clarification. The similarity in the patterns these very different discharge systems display, suggests that the patterns should be understandable in term of simplified models that do not include all of details of the fundamental dynamical equations.

Most of the theoretical investigations of the current patterns (for instance, [12–15]) are based on strongly phenomenological equations for the current-density distribution across the electrode surface. A second description of the current pattern formation has been developed on physical grounds for small deviations from a lateral-homogeneous state by using the experimentally or numerically defined current-voltage characteristic [16,17]. These approaches result in interesting static and dynamic patterns and were able to reproduce many patterns and scenarios observed experimentally in the laterally extended dc and ac discharge systems. Several phenomenological aspects of uniform glows and spots are, however, still uncertain, as are many details of their theory.

The main purpose of the present work is to obtain a simplified physically self-consistent model of the anode glow stratification in elevated-pressure parallel-plate dc discharges. Our principal assumption is that the asymptotically equivalent equations for the current-density and anode potential drop distributions on the anode surface are derivable from a basic (three-dimensional) fluid description of electron and ion transport coupled with Poisson's equation. In this paper we present a detailed investigation of this model, and show that it provides most of the basic features of a current pattern formation of the basic model.

The paper is comprised of six sections. In Sec. II a two-component reaction-diffusion system of activator-inhibitor-type is derived from a basic fluid description of charge transport in the discharge volume including both near-anode layer and positive column. Section III contains results from bifurcation analysis concerning the formation of spatially periodic stripe patterns. Section IV explores, analytically and numerically, the possible scenarios of instability evolution to the regular or irregular localized particlelike structures (stripes) of the near-anode plasmas. The properties of a single stripe and the normal current-density effect are discussed in Sec. V. Finally, in Sec. VI some conclusions are drawn.

II. BASIC EQUATIONS

The simplest set of equations containing the basic physics necessary for formation of constricted discharge structures are the well-known continuity equations in the drift-diffusion

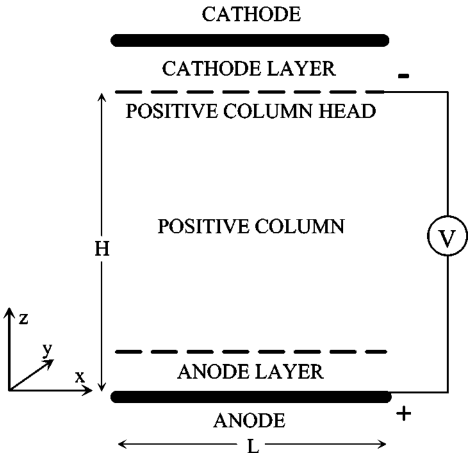

FIG. 1. Schematic diagram of the glow discharge used in this study. The gap between the anode and the positive column head defines the model region.

approximation for electrons and positive-ions coupled with Poisson's equation for the electric field, along with various constituent relations involving the discharge plasma coefficients

$$\frac{\partial n_j}{\partial t}+\boldsymbol{\nabla}\cdot\boldsymbol{\Gamma}_j=S_j,$$

$$\boldsymbol{\Gamma}_j=-D_j\boldsymbol{\nabla}n_j-\frac{q_j}{|q_j|}\mu_j n_j\boldsymbol{\nabla}\varphi, \tag{1}$$

$$\nabla^2\varphi=-\frac{1}{\varepsilon_0}\sum_j q_j n_j, \tag{2}$$

$$\mathbf{J}=\sum_j q_j\boldsymbol{\Gamma}_j,$$

where n_j is the particle density ($j=e$ or i for electrons and positive ions, respectively), μ_j, D_j, and q_j are their mobility, diffusivity, and charge, φ is the electric potential, $\mathbf{J}$ is the current density, and ε_0 is the permittivity of free space. In the case being considered, $S_e=S_i=n_e(\alpha-\beta n_i)$, where α is the frequency of direct ionization and β is the electron-ion recombination coefficient. The gas is assumed to be electropositive.

In most cases, the contraction of self-sustained quasistationary glow discharges at elevated-pressure gases is preceded by the formation of anode spots [1]. It seems reasonable to say that in many cases the formation of anode structures is relatively independent of the near-cathode processes [18]. That is why here the discharge region under study was chosen to be between the anode and the head of the positive column (see Fig. 1). Excluding the cathode region from consideration makes it possible to obtain a simplified physical self-consistent model of anode glow stratification and examine an array of problems that are not directly related to the conditions near the cathode, but are important in a number of technical applications characterized by an elongated, volumetrically uniform, positive column (such as in gas-discharge chambers with a thoroughly segmented cathode and a flat, solid anode [1]). That makes it possible to also avoid a number of difficulties related to the applicability of basic model (1) and (2) for describing regions of cathode drop, negative glow, and Faraday dark space.

The following boundary conditions have been taken: $\varphi=V$ ($V=\text{const}>0$), $\boldsymbol{\Gamma}_i\cdot\boldsymbol{\nu}=0$, $\boldsymbol{\Gamma}_e\cdot\boldsymbol{\nu}=\sigma_e n_e$ for the anode; $\varphi=0$, $\partial n_i/\partial\boldsymbol{\nu}=0$, $[\boldsymbol{\Gamma}_e+(\mu_e/\mu_i)\boldsymbol{\Gamma}_i]\cdot\boldsymbol{\nu}=0$ for the positive column head; $\partial n_e/\partial\boldsymbol{\nu}=\partial n_i/\partial\boldsymbol{\nu}=\partial\varphi/\partial\boldsymbol{\nu}=0$ for the lateral surfaces. In these cases, $\boldsymbol{\nu}$ is a unit vector with the external normal for the discussed surfaces, σ_e is the coefficient responsible for the electron flux interaction with the anode surface. The boundary condition for the electron flux in the positive column head is retained a typical form for the cathode (with the effective secondary emission coefficient $\gamma=\mu_e/\mu_i$), but it fulfills requirement of the quasineutrality $n_e=n_i$ when $\partial n_e/\partial\boldsymbol{\nu}=0$. The boundary conditions on the lateral surfaces ($x=0$ and $x=L$) maintain the conditions for the electron and ion impermeability. Thus the calculation region may be interpreted as a periodic pattern cell.

Anode and cathode spots have a complex, poorly understood morphology, even for the simple plane-parallel discharge geometry. Due to the severe nonlinearity and strong coupling of equations (1) and (2), the treatment of these equations is a difficult problem. We therefore restrict ourselves to a limited set of conditions, ignoring gas heating, plasma chemistry, and nonlinear surface effects. However, these factors can become more important as the current increases.

The local field approximation is used to obtain the ionization rate. It is assumed that the ionization rate depends on the local coordinates only through the normalized local electric field E/p, where $E=|\boldsymbol{\nabla}\varphi|$ is the magnitude of the field and p is the gas pressure. The ionization term is a very strong function of the value of E/p, and this has played a dominant role in the case under consideration. To simplify the calculation and analysis, the electron and ion mobilities and diffusion coefficients are assumed to be field independent and the ratio D_e/μ_e for electrons is chosen as a parameter (effectively the electron temperature).

The system of equations (1) and (2) can be rewritten as

$$\nabla^2\varphi=-\gamma\rho, \tag{3}$$

$$\partial\rho/\partial t+\boldsymbol{\nabla}\cdot\boldsymbol{\Gamma}=0,$$

$$\boldsymbol{\Gamma}=(D_e-D_i)\boldsymbol{\nabla}n_e-D_i\boldsymbol{\nabla}\rho-(\mu_e+\mu_i)n_e\boldsymbol{\nabla}\varphi-\mu_i\rho\boldsymbol{\nabla}\varphi, \tag{4}$$

$$\frac{\partial}{\partial t}(n_e+\theta\rho)-D_s\nabla^2 n_e-\theta D_i\boldsymbol{\nabla}^2\rho-\theta\mu_i\boldsymbol{\nabla}\cdot(\rho\boldsymbol{\nabla}\varphi)$$
$$=n_e[\alpha-\beta(n_e+\rho)], \tag{5}$$

$$\mathbf{J}=e\boldsymbol{\Gamma},$$

where $\gamma\equiv e/\varepsilon_0$, $\rho\equiv n_i-n_e$ is the charge density (in unsigned electronic charge unit e), $\theta\equiv\mu_e/(\mu_e+\mu_i)$, and $D_s\equiv(\mu_e D_i+\mu_i D_e)/(\mu_e+\mu_i)$ is the ambipolar diffusion coefficient. Equation (4) is the charge conservation equation.

Equation (5) is the sum of Eq. (1) for the electrons and the positive ions multiplied by factors $\theta\mu_i/\mu_e$ and θ, respectively.

Integrating Eqs. (3)–(5) over the longitudinal coordinate z, we obtain equations for the averaged electron density $N \equiv (1/H)\int_0^H n_e\,dz$ and the anode potential drop $U \equiv \int_0^H (E_z - E_p)\,dz$. Hereafter, we will use the subscript z to denote the longitudinal component of a variable and a its value on the anode $(z=0)$, and p its value at the positive column head $(z=H)$. Note that $\rho\to 0$ and $E_z - E_p \to 0$ asymptotically as $z\to H$ [19].

Multiplying Eq. (4) by a factor z and integrating over z between anode $(z=0)$ and positive column head $(z=H)$, we obtain

$$\frac{\partial}{\partial t}\int_0^H \rho z\,dz + \boldsymbol{\nabla}_\perp\cdot\int_0^H z\boldsymbol{\Gamma}_\perp\,dz + \int_0^H z\frac{\partial \boldsymbol{\Gamma}_z}{\partial z}\,dz = 0, \tag{6}$$

where the subscript $\perp$ denotes the transverse component of variable or operator.

The first integral in Eq. (6) is given by

$$\begin{aligned}\int_0^H \rho z\,dz &= -\frac{1}{\gamma}\int_0^H (\varphi''_{zz} + \nabla_\perp^2\varphi)z\,dz\\ &= -\frac{U}{\gamma} + \frac{H^2}{6\gamma}\nabla_\perp^2[(1-\overline{X_E^2})U],\end{aligned} \tag{7}$$

where $\overline{X_E^m} \equiv (1+m)\int_0^H (E_z - E_p)(z/H)^m dz / \int_0^H (E_z - E_p)\,dz$ (with $m=2$ in this case) is the appropriate dimensionless thickness of anode sheath.

Note also that

$$U = (E_s - E_p)H, \tag{8}$$

where $E_s \equiv V/H$ is the average electric field.

The next term in Eq. (6) is defined by

$$\begin{aligned}\boldsymbol{\nabla}_\perp\cdot\int_0^H z\boldsymbol{\Gamma}_\perp\,dz &= \nabla_\perp^2\int_0^H [(D_e - D_i)n_e - D_i\rho]z\,dz\\ &\quad - \boldsymbol{\nabla}_\perp\cdot\int_0^H [(\mu_e+\mu_i)n_e + \mu_i\rho]\boldsymbol{\nabla}_\perp\varphi z\,dz\\ &\simeq \frac{H^2}{2}(D_e - D_i)\nabla_\perp^2 N + \frac{D_i}{\gamma}\nabla_\perp^2[(1-\overline{X_E^2})U]\\ &\quad + \frac{H^2}{6}(\mu_e+\mu_i)\nabla_\perp\cdot\{N\nabla_\perp[(1-\overline{X_E^2})U]\}\\ &\quad - \frac{\mu_i}{4\gamma}\nabla_\perp^2[(1-\overline{X_E})U^2],\end{aligned}$$

where $\overline{X_E} \equiv \overline{X_E^m}$ with $m=1$.

The last term in Eq. (6) is given by

$$\int_0^H z\frac{\partial \Gamma_z}{\partial z}\,dz = (\Gamma_p - \overline{\Gamma})H,$$

where the averaging over z is denoted by the vinculum.

Thus we have the equation for the anode potential drop U

$$\begin{aligned}\frac{\partial U}{\partial t} - \frac{H^2}{6}\frac{\partial}{\partial t}\nabla_\perp^2[(1-\overline{X_E^2})U] &\simeq \frac{\gamma H^2}{2}(D_e - D_i)\nabla_\perp^2 N\\ &\quad + \frac{\gamma H^2}{6}(\mu_e+\mu_i)\boldsymbol{\nabla}_\perp\cdot\{N\nabla_\perp[(1-\overline{X_E^2})U]\}\\ &\quad + D_i\nabla_\perp^2 U - \frac{\mu_i}{4}\nabla_\perp^2[(1-\overline{X_E})U^2] - f_U,\end{aligned} \tag{9}$$

where $f_U \equiv \gamma H(\overline{\Gamma} - \Gamma_p)$ and $\overline{\Gamma} \equiv (1/H)\int_0^H \Gamma_z dz$.

Further averaging Eq. (5) over z, we get

$$\begin{aligned}&\frac{\partial}{\partial t}(N + \theta\overline{\rho}) - D_s\nabla_\perp^2 N - \theta D_i\nabla_\perp^2\overline{\rho} - \theta\mu_i\boldsymbol{\nabla}_\perp\cdot\overline{(\rho\boldsymbol{\nabla}_\perp\varphi)}\\ &\quad - \frac{1}{H}\left(D_s\frac{\partial n_e}{\partial z} + \theta D_i\frac{\partial\rho}{\partial z} - \theta\mu_i\rho E_z\right)\Bigg|_0^H\\ &= \overline{n_e[\alpha - \beta(n_e+\rho)]}.\end{aligned}$$

The ionization term is a very strong function of the value of E/p. Hence, assuming that $(E_a/E_p)n_e|_a \simeq n_e|_p \simeq N$, the term on the right side of the equation can be written as

$$\overline{n_e[\alpha - \beta(n_e+\rho)]} \simeq N\frac{E_p}{E_a}\overline{\alpha - \alpha_p} + N(\alpha_p - \beta N) - \beta N\overline{\rho}.$$

Taking into account the boundary conditions and the estimation $2\gamma\boldsymbol{\nabla}_\perp\cdot\overline{(\rho\boldsymbol{\nabla}_\perp\varphi)} \simeq \nabla_\perp^2\overline{E_z^2}$ we have

$$\frac{\partial}{\partial t}(N + \theta\overline{\rho}) \simeq D_s\nabla_\perp^2 N + \theta D_i\nabla_\perp^2\overline{\rho} + \frac{\theta\mu_i}{2\gamma}\nabla_\perp^2\overline{E_z^2} - f_N, \tag{10}$$

where $f_N \equiv N((\theta\mu_i/H)E_p - (E_p/E_a)\overline{\alpha - \alpha_p} - \alpha_p + \beta N + \beta\overline{\rho})$. Because $\overline{J}/N \simeq e(\mu_e+\mu_i)E_s = \text{const}$, this equation governs in essence the current-density distribution on the anode surface. Previously Eq. (10) was successfully employed to describe the peripheral part of the current structures [4].

The term $\overline{\alpha - \alpha_p}$ can be approximated by the product of the average value of $\alpha - \alpha_p$ and the ratio of average anode sheath thickness X to H. These average values we will calculate with the weight function $h(z) = \rho(z)/\int_0^H \rho(z)\,dz$. In that event the thickness X is defined as the characteristic quasineutrality breakdown dimension in the near-anode region $X_\rho = \|z\|_\rho \equiv \int_0^H z\rho\,dz/\int_0^H \rho\,dz$. Therefore,

$$\overline{\alpha - \alpha_p} = \frac{\lambda_\rho}{H}||\alpha - \alpha_p||_\rho\,||z||_\rho = -\frac{\lambda_\rho X_\rho}{\gamma H^2\overline{\rho}}\int_{E_p}^{E_a}(\alpha - \alpha_p)\,dE,$$

where λ_ρ is an unknown parameter of the order of unity.

The average charge in the near-anode plasma is equal to

$$\overline{\rho}=-\frac{1}{\gamma H}\int_0^H(\varphi''_{zz}+\nabla_\perp^2\varphi)dz$$

$$=-\frac{1}{\gamma H}(E_a-E_p)+\frac{1}{2\gamma}\nabla_\perp^2[(1-\overline{X_E})U].$$

As a rule the anode sheath thickness is considerably less than the discharge gap (i.e., X_ρ/H, $\overline{X_E}$,$\overline{X_E^2}\ll 1$) and $\overline{\rho}\ll N$, hence Eqs. (9) and (10) may be simplified to

$$\frac{\partial N}{\partial t}\simeq D_s\nabla_\perp^2 N+\frac{\theta\mu_i}{2\gamma H}\nabla_\perp^2[(E_a-E_s)U]-\frac{\beta N}{2\gamma}\nabla_\perp^2 U-f_N, \tag{11}$$

$$\frac{\partial U}{\partial t}-\frac{H^2}{6}\frac{\partial}{\partial t}\nabla_\perp^2 U\simeq\frac{\gamma H^2}{2}(D_e-D_i)\nabla_\perp^2 N+\frac{\gamma H^2}{6}\times\nabla_\perp\left\{\left[\frac{6D_i}{\gamma H^2}+(\mu_e+\mu_i)N\right]\boldsymbol{\nabla}_\perp U\right\}-f_U, \tag{12}$$

where $f_N=N[(\theta\mu_i/H)E_p+(\lambda_\rho X_\rho E_p/\gamma H^2\overline{\rho}E_a)\int_{E_p}^{E_a}(\alpha-\alpha_p)dE-\alpha_p+\beta N]$. If we replace the average value of Γ by its half-sum at the anode and positive column head [i.e., $\overline{\Gamma}\simeq(\Gamma_a+\Gamma_p)/2$], we obtain $f_U\simeq(\gamma H/2)(\Gamma_a-\Gamma_p)$. The small value $6D_i/(\gamma H^2)$ provides a strongly parabolic condition for Eq. (12) as $N\rightarrow 0$.

In order to get a completed self-consistent model we use asymptotic results [19] for Γ_a and E_a. The presence of the small parameter $\varepsilon=X_u/H$, with $X_u=D_e/(\mu_e E_a)$ being the relaxation length of the spatial disturbance scale due to diffusion electron leakage to the anode, makes it possible to use an asymptotic method for constructing an approximate solution of the problem for the laterally homogeneous state. The use of these asymptotic results is generally based on the assumption that the longitudinal distributions of the electrical field and electron and ion densities are scarcely affected by transverse charge fluxes if the current density J is fixed for the position x under consideration. The fact, that the thickness of near-anode layer is usually much less than the transverse dimensions of current structures, supports the validity of this assumption. According to Eqs. (3.7) and (3.9) in Ref. [19] (for comparison see also Eqs. (34) and (37) in [20] for electronegative gases) the leading (nonperturbed) terms for Γ_a and E_a may be determined by using

$$\Gamma_a=\frac{2\mu_e}{\gamma\psi\mu_i}\int_{E_p}^{E_a}(\alpha-\alpha_p)dE, \tag{13}$$

$$U=\chi\frac{E_a}{E_p}\frac{(E_a-E_p)^2}{\gamma N}, \tag{14}$$

where $\chi\equiv 1+\alpha_1+2\alpha_2+\cdots$, $(1, \alpha_1, \alpha_2, \ldots$ designate the coefficients of asymptotic expansion of an integral in a series with the small parameter $\delta=1-E_p/E_a)$, $\psi\equiv 2(\mu_e^2/\mu_i^2)[\mu_i/\mu_e-\ln(1+\mu_i/\mu_e)]$ ($\psi\simeq 1$ for $\mu_i/\mu_e\ll 1$).

Using Eq. (13), we get

$$f_U=\frac{H\mu_e}{\psi\mu_i}\int_{E_p}^{E_a}(\alpha-\alpha_p)dE-\frac{\gamma H\mu_e}{2}NE_p. \tag{15}$$

It now follows that

$$f_N=-\frac{2\theta\mu_i}{\gamma H^2\mu_e}f_U+\frac{\Pi}{\gamma H}\int_{E_p}^{E_a}(\alpha-\alpha_p)dE-N(\alpha_p-\beta N),$$

where $\Pi\equiv 2\theta/\psi+\lambda_\rho X_\rho E_p N/H\overline{\rho}E_a$. It is clear that the values N and E_p for lateral-homogeneous states of the model under study and for the asymptotic model [19] are necessarily identical. Therefore, $\Pi=0$ [this means that $\lambda_\rho\simeq 2\theta/(\chi\psi)$], so that

$$f_N=-\frac{2\theta\mu_i}{\gamma H^2\mu_e}f_U-N(\alpha_p-\beta N). \tag{16}$$

The system of reaction-diffusion equations (11) and (12) with Neuman (no-flux) boundary conditions, where the source terms f_U and f_N are given by Eqs. (15) and (16) and the coefficients E_a and E_p are defined from Eqs. (8) and (14), respectively, constitute the full set of equations of the model.

The above results, obtained by means of the asymptotic expansion in terms of the small parameters, relate to the case in which a thin boundary layer develops because of the electron diffusion, but the profile of plasma parameters inside the relatively thicker anode sheath is basically determined by the breakdown of quasineutrality. From the comparison between X_u and $X_\rho\simeq U/(E_a-E_p)$ we find that this corresponds to the condition

$$\frac{D_e}{\mu_e}\left(1-\frac{E_p}{E_a}\right)\ll U. \tag{17}$$

Condition (17) can be rewritten as

$$\Gamma\ll\frac{2\mu_e^2}{\gamma D_e}E_a^2(E_a-E_p). \tag{18}$$

Another limitation arises because of the condition $\overline{X_E}\ll 1$ used for Eq. (12) that can be written as

$$\Gamma\gg\frac{16\mu_e}{\gamma H}E_a(E_s-E_p). \tag{19}$$

In accordance with the most commonly encountered approximations, the dependence of α on the electric field E can be represented in the form

$$\alpha=A(E/B)^r\exp(-B/E), \tag{20}$$

where A/p, B/p, and r are constants for a given gas, p is gas pressure. If so, changing to dimensionless independent variables according to

$$n=\frac{\gamma\mu_i}{2A}N,\quad u=\frac{U}{HB},\quad F=\frac{E}{B},\quad \tilde{t}=At, \tag{21}$$

$$\tilde{x}=\sqrt{\frac{A}{D_s}}x, \quad \left(\text{i.e.,} \nabla_\perp \equiv \frac{\partial}{\partial \tilde{x}} \quad \text{and } l=\sqrt{\frac{A}{D_s}}L\right),$$

and defining

$$\tilde{\alpha}=\frac{\alpha}{A}, \quad \tilde{\beta}=\frac{2\beta}{\gamma\mu_i}, \quad \xi=\frac{\mu_i}{\mu_e},$$

$$\vartheta=\frac{D_i}{D_e}, \quad h=\frac{HA}{2B\mu_i}, \quad w=\sqrt{\frac{H^2A}{3D_s}}, \tag{22}$$

we obtain the final system of equations

$$\frac{\partial n}{\partial \tilde{t}} \simeq \nabla_\perp^2 n+\frac{1}{2h}f_u-f_n, \quad f_n=-n(\tilde{\alpha}_p-\tilde{\beta}n); \tag{23}$$

$$\xi\frac{\partial u}{\partial \tilde{t}} \simeq \boldsymbol{\nabla}_\perp \cdot [(\vartheta+w^2 n)\boldsymbol{\nabla}_\perp u]-f_u,$$

$$f_u=\int_{F_p}^{F_a}(\tilde{\alpha}-\tilde{\alpha}_p)dF-nF_p; \tag{24}$$

$$\left.\frac{\partial n}{\partial \tilde{x}}\right|_{\tilde{x}=0,l}=\left.\frac{\partial u}{\partial \tilde{x}}\right|_{\tilde{x}=0,l}=0 \tag{25}$$

with

$$F_a \simeq F_p+\sqrt{hnu} \tag{26}$$

and

$$F_p=F_s-u. \tag{27}$$

In this final system we use the simplified solution (26) for Eq. (14) and drop terms with little importance at conditions of interest to us.

The integral in Eq. (24) is expressed by the equation

$$\int_{F_p}^{F_a}(\tilde{\alpha}-\tilde{\alpha}_p)dF=\Gamma\left(-1-r,\frac{1}{F_a}\right)-\Gamma\left(-1-r,\frac{1}{F_p}\right)$$
$$-\tilde{\alpha}_p(F_a-F_p), \tag{28}$$

where $\Gamma(a,y)\equiv\int_y^\infty e^{-t}t^{a-1}dt$ is the complementary incomplete gamma function. For the case of large values of $y+1-a$ considered the expansion [21]

$$\Gamma(a,y)=\frac{e^{-y}y^a}{y+1-a}\sum_{k=0}^{\infty}\frac{g_k(y)}{(y+1-a)^{2k}},$$

$$g_{k+1}(y)=(1-a-2ky)g_k(y)+y(y+1-a)\frac{\partial}{\partial y}g_k(y),$$

$$g_0=1$$

may be used. Retaining in Eq. (28) only the principal term of the asymptotic expansion, with good accuracy we have

$$\int_{F_p}^{F_a}(\tilde{\alpha}-\tilde{\alpha}_p)dF \simeq \frac{\tilde{\alpha}_aF_a}{2+r+1/F_a}-\frac{\tilde{\alpha}_pF_p}{2+r+1/F_p}$$
$$-\tilde{\alpha}_p(F_a-F_p). \tag{29}$$

If both $\beta p=\text{const}$ and $Hp=\text{const}$, the dimensionless variables and all parameters of model (23)–(25) are p independent and the present model obeys similarity laws in physical space with invariants tp, xp, U, E/p, and J/p^2.

III. LINEAR STABILITY ANALYSES

Under discharge voltage control, i.e., fixed control parameter F_s, the model described by Eqs. (23)–(25) has at least a trivial equilibrium state $n=0$ (no current flows). In addition, saddle-node bifurcation occurs at $F_s=F_*$ and a pair of the homogeneous fixed points (n_1,U_1) and (n_2,U_2) arises as $F_s>F_*$ [see Fig. 2(a)]. We will use the parameter F_s as the bifurcation parameter. In terms of the basic model the quantities n and F_s correspond to the current density and discharge voltage, respectively, which are physical quantities of interest. Thus Fig. 2(a) shows the normalized static current-voltage characteristic. The model predicts the negative slope of the curve $u(n)$ in accordance with experiment [22] in air and N_2 and only a slight fall in u with a rise in the electron-ion recombination coefficient β (Fig. 3). Since $\partial n/\partial F_s=\infty$ as $F_s=F_*$, it follows that F_* is given by the equation

$$\Omega=0,$$

where

$$\Omega\equiv\frac{\partial f_n}{\partial n}\frac{\partial f_u}{\partial u}-\frac{\partial f_u}{\partial n}\frac{\partial f_n}{\partial u}. \tag{30}$$

The root of this equation can be obtained iteratively

$$F_* \simeq g+\frac{g^2}{1-4g}+\frac{2g^3}{1-4g}\sqrt{\frac{h}{\tilde{\beta}}}\exp\left(-\frac{1}{2g}\right),$$

where g is the solution of the equation

$$\tilde{\beta}G^2\ \exp\left(-\frac{1}{G}\right)=g\ \exp\left(-\frac{1}{g}\right)$$

with

$$G(g)\equiv g+\sqrt{\frac{h}{(1-4g)\tilde{\beta}}}g\ \exp\left(-\frac{1}{2g}\right).$$

Then the bifurcation point (n_*,u_*) is defined as $[\exp(-1/g)/\tilde{\beta},F_*-g]$.

First we study the trivial equilibrium state $(n,u)=(0,0)$. To perform a stability analysis, we linearize the dynamic system (23) and (24) around this spatially homogeneous fixed point for small space- and time-dependent fluctuations $(\delta n,\delta u)=[\tilde{n}\exp(i\tilde{q}\tilde{x}),\tilde{u}\exp(i\tilde{q}\tilde{x})]$, and obtain the set of equations

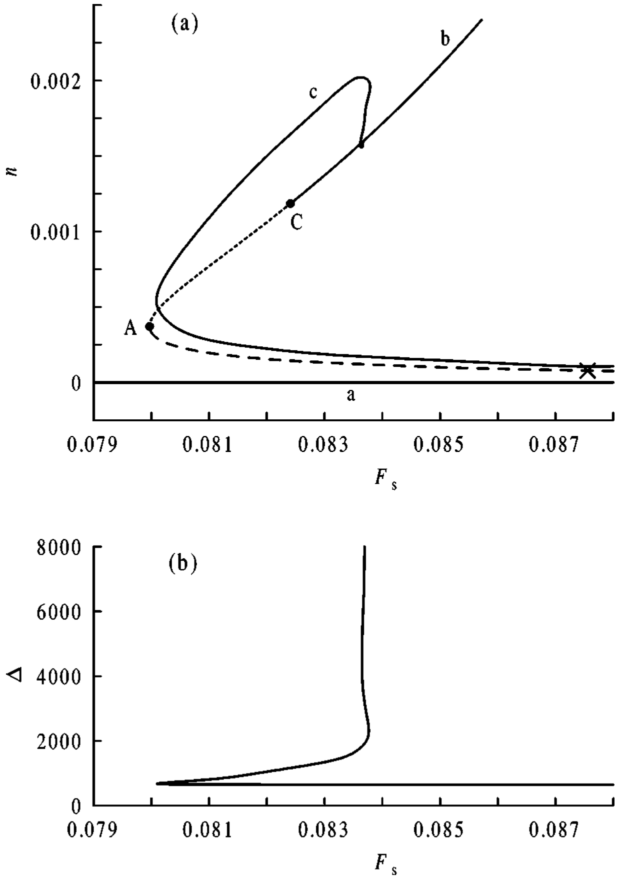

FIG. 2. (a) Bifurcation diagram in the plane (n,F_s) for model (23) and (24). Curves *a* and *b* show F_s dependence of *n* for trivial and bifurcation solutions, respectively. Solid, dashed, and dotted lines indicate stable, absolute unstable, and Turing unstable equilibrium states, respectively. The instability region of the trivial solution (i.e., $F_s>F_0=0.093\,14$) lies exterior to the plot. Points *A* and *C* mark the saddle-node bifurcation and the critical point of the Turing instability, respectively. Point × is referred to in Fig. 5. Curve *c* shows F_s dependence of n_0 for solution in the form of a single localized stationary stripe, where $n_0=n$ at the middle of this stripe. (b) F_s-dependence of the dimensionless transverse size $\Delta=\int n d\tilde{x}/n_0$ of this stripe. Parameters of the model are $h=2142.9$, $\tilde{\beta}=0.002526$, $w=2128.3$, $\xi=0.003\,889$, and $\vartheta=0.000\,100\,6$.

$$\frac{\partial\tilde{n}}{\partial\tilde{t}}=\tilde{n}(a+\gamma\tilde{n}+\delta\tilde{u}+Q), \tag{31}$$

$$\frac{\partial\tilde{u}}{\partial\tilde{t}}=\tilde{n}(c+\beta\tilde{u}+R)+d\tilde{u} \tag{32}$$

with

$$a=\alpha_s-\frac{F_s}{2h}-\tilde{q}^2,\quad \gamma=-\tilde{\beta},\quad \delta=-\frac{1}{2h}+\frac{3\alpha_s}{4F_s^2},$$

$$c=\frac{F_s}{\xi},\quad d\equiv-\frac{\vartheta}{\xi}\tilde{q}^2,\quad \beta=\frac{1}{\xi}+\frac{h\alpha_s}{2\xi F_s^2},$$

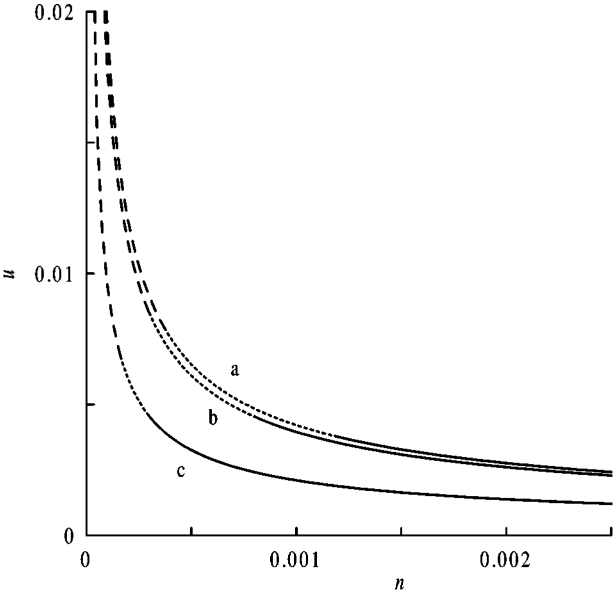

FIG. 3. Dimensionless anode voltage drop *u* versus averaged electron density *n*. Solid, dashed, and dotted lines indicate stable, absolute unstable, and Turing unstable solutions, respectively. Curve *a* is calculated for parameters as in Fig. 2. Curves *b* and *c* are calculated at double $\tilde{\beta}$ and *h*, respectively.

where *Q* and *R* are free from terms of degree below two, $\alpha_s\equiv\tilde{\alpha}(F_s)=F_s^r\exp(-1/F_s)$.

The linear part of Eqs. (31) and (32) yields the eigenvalues

$$\lambda_1=a,\quad \lambda_2=d.$$

Modes with $\lambda>0$ are unstable. Since $d\leqslant 0$, the instability condition is $a>0$. The Neumann boundary conditions (25) allow only cosine modes $\cos(\tilde{q}\tilde{x})$, where $\tilde{q}=k\pi/l$ with integer *k*. The asymptotic stability condition is $a<0$, with one exception when $k=0$. For the critical case $\lambda_2=0$ (i.e., for the homogeneous mode $k=0$) we can do the standard stability analysis by Lyapunov's second (direct) method. Let us consider the function

$$W=\tilde{n}^2+\left(\frac{c}{a}\tilde{n}-\tilde{u}\right)^2. \tag{33}$$

According to Eqs. (31) and (32), we get

$$\frac{\partial W}{\partial\tilde{t}}=2a\tilde{n}^2+\tilde{n}O((|\tilde{n}|+|\tilde{u}|)^2). \tag{34}$$

We have from Eq. (34) that $\partial W/\partial\tilde{t}<0$ if $a<0$, asserting stability of solution for small $\tilde{n}$ and $\tilde{u}$ [23]. In the converse case, when $a>0$, the solution is unstable.

Thus for $F_s<F_0$, where F_0 is the least positive root of the equation $a(k=0)=0$ [i.e., $F=2h\tilde{\alpha}(F)$], the trivial solution is stable against any small perturbations. In this case the ionization is small and the perturbations are removed from near-anode layer owing to the charge flows. However, for

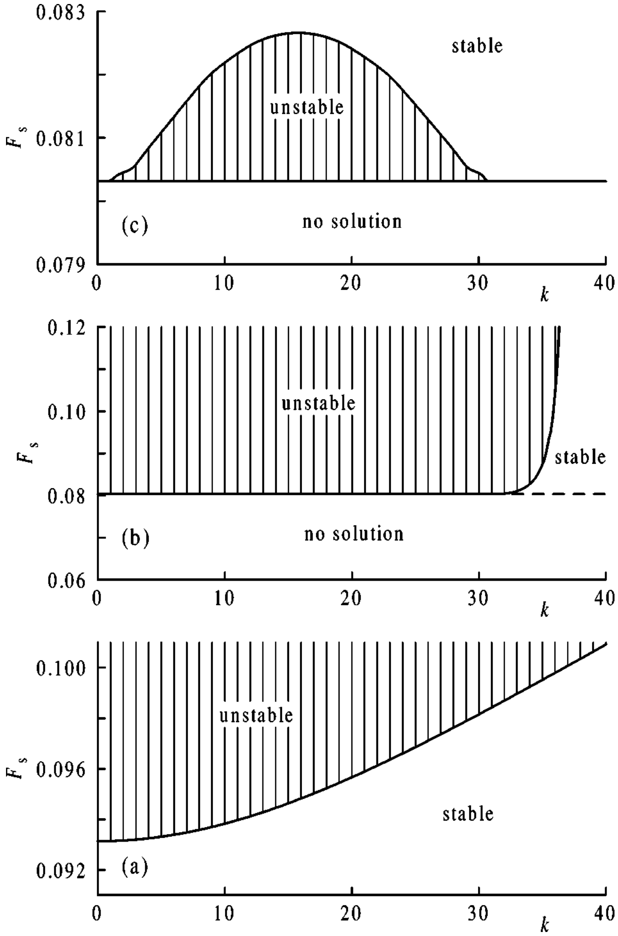

FIG. 4. Linear stability diagrams for (a) trivial, (b) lower, and (c) higher branches resulting from Eqs. (23)–(25). Bifurcation parameter F_s is plotted against the dimensionless wave number k. Vertical lines indicate allowed discrete values of k for a system constrained by no-flux boundary conditions (i.e., $k=\tilde{q}l/\pi$). Parameters are as in Fig. 2 and additionally $l=245\,75$.

$F_s > F_0$ ionization dominates over other processes and the system becomes unstable. Figure 4(a) describes various possibilities concerning the first bifurcation of the trivial equilibrium state.

Second, we study the equilibrium states (n_1, U_1) and (n_2, U_2) for $F_s > F_*$. Analysis of Eqs. (23) and (24) revealed that typically the variable n acts as an activator and u acts as an inhibitor in terms of nonlinear dynamics [24]. To perform a stability analysis, we linearize the dynamic system (23) and (24) around spatially homogeneous fixed points for small space- and time-dependent fluctuations $(\delta n, \delta u) \sim \exp(\tilde{\lambda}\tilde{t} + i\tilde{q}\tilde{x})$ and obtain the characteristic equation

$$\xi\lambda_k^2 - \lambda_k(\xi p_k - v_k) - \left(\frac{\partial f_n}{\partial u} - \frac{1}{2h}\frac{\partial f_u}{\partial u}\right)\frac{\partial f_u}{\partial n} - p_k v_k = 0, \tag{35}$$

where for no-flux conditions (25) (i.e., $\tilde{q} = k\pi/l$ with integer k) the coefficients are defined by

$$p_k = \frac{1}{2h}\frac{\partial f_u}{\partial n} - \frac{\partial f_n}{\partial n} - \frac{\pi^2}{l^2}k^2,$$

$$v_k = \frac{\partial f_u}{\partial u} + (\vartheta + w^2 n)\frac{\pi^2}{l^2}k^2.$$

The roots of Eq. (35) yield the dispersion relation

$$\lambda_{k(1,2)} = \frac{\xi p_k - v_k}{2\xi} \pm \frac{1}{2\xi}\left[(\xi p_k + v_k)^2 + 4\xi\left(\frac{\partial f_n}{\partial u} - \frac{1}{2h}\frac{\partial f_u}{\partial u}\right)\frac{\partial f_u}{\partial n}\right]^{1/2}. \tag{36}$$

We see that as $k \to \infty$, $(\xi p_k + v_k)^2 \to (\vartheta + w^2 n - \xi)^2 \pi^4 k^4 / l^4 \to \infty$. Thus, $\lambda_{k(1,2)}$ is necessarily real for a large k. However λ_k may be complex on the lower branch for $F_s \gg F_*$ when $w^2 n < \xi - \vartheta$ and $\xi p_k + v_k \simeq 0$.

Modes with $\mathrm{Re}(\lambda_k) > 0$ are unstable. As is easy to see from Eq. (36), this requires

$$\xi p_k - v_k > 0 \tag{37}$$

or

$$\left(\frac{\partial f_n}{\partial u} - \frac{1}{2h}\frac{\partial f_u}{\partial u}\right)\frac{\partial f_u}{\partial n} + p_k v_k > 0. \tag{38}$$

Inequality (37) may be valid on the lower branch for a large F_s when $F_a + F_p < 2F_s$ and $\partial f_u / \partial u < 0$. In the case of $k=0$ inequality (38) is true if $\Omega < 0$, i.e., on the whole lower branch. It is important that inequality (38) also will be valid on the part of the higher branch $(\Omega > 0)$ in range of k around a finite value $k = k_c$ (Turing instability). This is fulfilled if

$$(\vartheta + w^2 n)\left(\frac{\partial f_n}{\partial n} - \frac{1}{2h}\frac{\partial f_u}{\partial n}\right) + \frac{\partial f_u}{\partial u} < -2[(\vartheta + w^2 n)\Omega]^{1/2}. \tag{39}$$

Since the right part of inequality (39) peaks at $F_s = F_*$ and decreases drastically with increasing F_s, it follows that a Turing instability occurs only in a limited range $F_* < F_s < F_c$ and characterized at $F_s = F_c$ by the intrinsic dimensionless wave number k_c with

$$k_c = \frac{l}{\pi}\left(\frac{\Omega}{\vartheta + w^2 n}\right)^{1/4}. \tag{40}$$

Figures 4(b) and 4(c) describe various possibilities concerning the first bifurcation of the lower and higher branches of the equilibrium state, respectively. Figure 2(a) depicts the stable (solid lines), absolutely (saddle) unstable (dashed lines), and Turing unstable (dotted lines) modes. We see that model (23)–(25) has two stable equilibrium states over a certain range of F_s and thus it is a bistable system.

For a given F_s the zero eigenvalues $\lambda_k = 0$ are generally simple, except for some exceptional values of parameters in the case of the Turing instability. Thus, the points on curves in Figs. 4(a) and 4(b) corresponding to integer values of k are

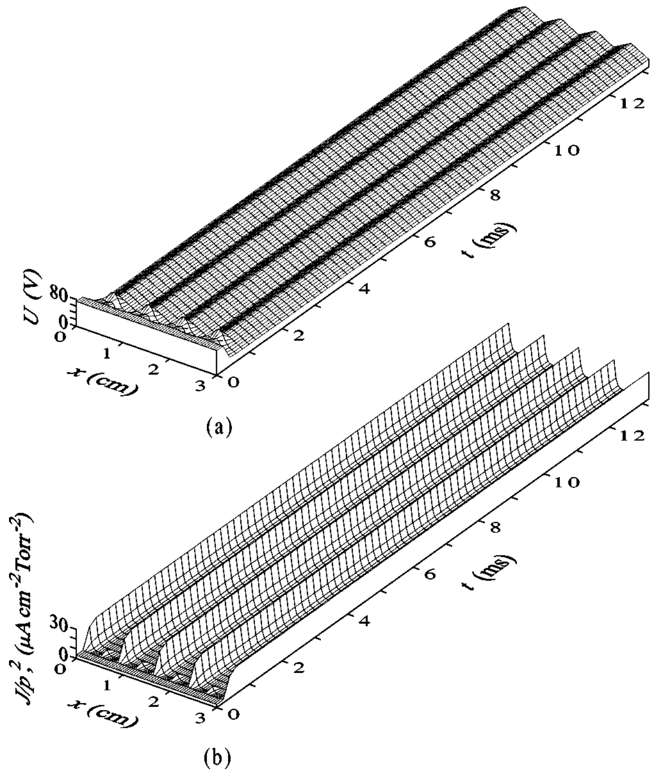

FIG. 5. Space and time variations of (a) anode voltage drop U and (b) normalized current density J/p^2 for the mean current density $\overline{J}=5$ mA/cm^2. Physical parameters of the model are $p=40$ Torr, $D_e/\mu_e=1$ eV, $\beta=1\times10^{-7}$ cm^3/s, $L=3$ cm, and $H=0.45$ cm. The initial homogeneous state is marked × in Fig. 2.

necessarily bifurcation points of equilibrium states. For completeness, we obtain the conditions under which in the case of the Turing instability the eigenvalue λ_k is doubly degenerate. From Eq. (36) and $\lambda_k=\lambda_{k+m}=0$, we get that this rather exceptional condition may be written as

$$\frac{l^2\Omega^{1/2}}{\pi^2(\vartheta+w^2n)^{1/2}}=k(k+m),$$

where m is a positive integer. The problem of degenerate eigenvalues is beyond the scope of our present work.

IV. SPATIOTEMPORAL DYNAMICS IN THE MODEL

To verify the model, we have made some numerical calculations starting from the same conditions as in Ref. [25] where model (1)–(2) has been applied for investigations of the anode glow. Thus in the results presented below, $H=0.45$ cm and the gas mixture N_2:He$=1:1$ at $p=40$ Torr with the transport coefficients $A/p=7.5\times10^7$ s^{-1} Torr^{-1}, $B/p=180$ V cm^{-1} Torr^{-1}, $r=0$, $\mu_e p=4.5\times10^5$ cm^2 Torr s^{-1} V^{-1}, $\mu_i p=1.75\times10^3$ cm^2 Torr s^{-1} V^{-1}, $\beta=1\times10^{-7}$ cm^3/s, $D_i/\mu_i=0.026$ eV, and $D_e/\mu_e=1$ eV has been used as a working gas. The bifurcation diagram in Fig. 2 just confirms to this conditions.

As expected, the model shows similar patterns as in [25] (see Figs. 5 and 6). Here, in the homogeneous initial datum (point × on Fig. 2) we introduced small-amplitude (0.1%) perturbations whose spatial period was 0.75 cm. The discharge voltage $V(t)$ is preassigned to meet a given value of the mean current density $\overline{J}(t)\equiv\int J dx/\int dx=5$ mA/cm^2. We observed the growth of these perturbations and the formation of a periodic current structure. Looking at details, one observes certain differences between the behavior of solutions of Eqs. (23) and (25) and basic equations (1) and (2). In particular, in Fig. 5 the spatiotemporal dynamic calculated for $D_e/\mu_e=1$ eV holds the spatial regularity. The spatiotemporal dynamics of solutions of the basic equations are regular only for $D_e/\mu_e\lesssim0.7$ eV. Nevertheless the model also shows secondary bifurcations for $D_e/\mu_e=2$ eV (Fig. 6). A similar disruption of regularity is seen in experiments [4,2]. In addition we observe serious differences in the shape of U as $J\to0$ [see Fig. 5(a)] because of limitation (19) (i.e., when $X_\rho\to L$). Detailed consideration of the positive column revealed that at the middle of a stationary stripe ionization and recombination processes balance each other locally to a high accuracy in both models.

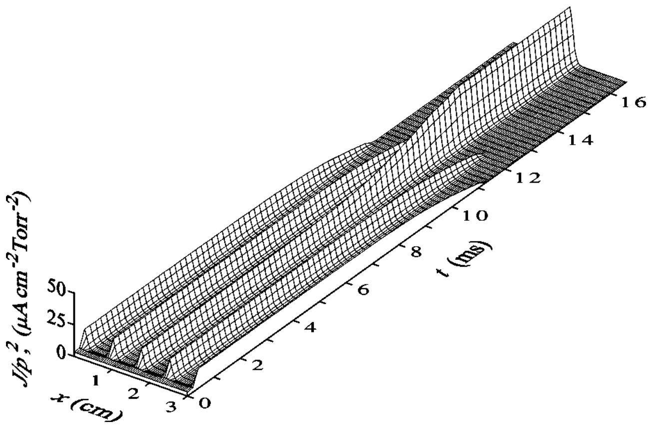

FIG. 6. Space and time variation of the normalized current density J/p^2 for the same conditions as in Fig. 5 with one exception, namely, $D_e/\mu_e=2$ eV.

Figure 7 shows the spatiotemporal dynamic in the absence of any special initiating perturbations for structure develop-

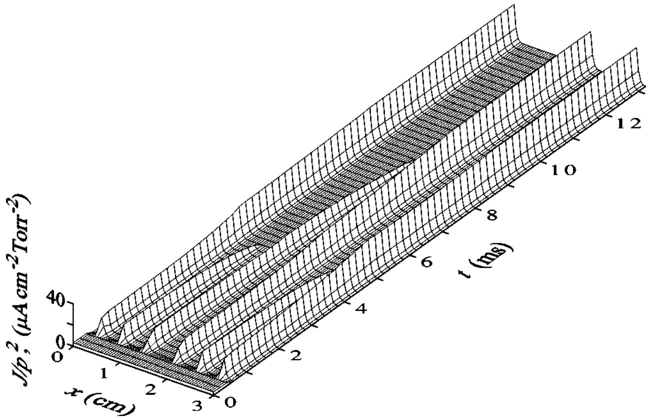

FIG. 7. Space and time variation of the normalized current density J/p^2 for the same conditions as in Fig. 5 with one exception, namely, in absence of any special initiating perturbations.

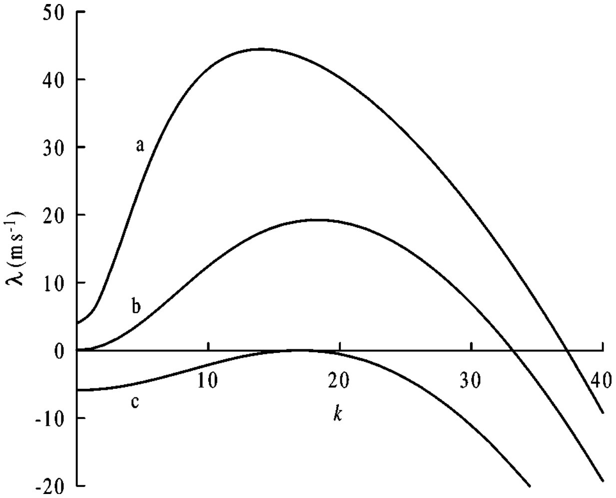

FIG. 8. Curves *a*, *b*, and *c* show dependences of the largest dimensional eigenvalue λ on the dimensionless wave number *k* ($k = qL/\pi$ because of no-flux boundary conditions) for the initial condition [point × in Fig. 2(a)], saddle-node point [point *A* in Fig. 2(a)], and critical point of the Turing instability [point *C* in Fig. 2(a)], respectively. All other conditions were the same as in Fig. 5.

ment. We observe that spontaneous perturbations freely grow because a finite number of decimal places in calculation and a nonzero tolerance of the iteration procedures. In simulation there is an initial delay of the order of a few hundred microsecond before the current structures start to develop, and a rapid growth the perturbations in the amplitude. This delay is in rough agreement with those experimentally obtained in elevated-pressure dry and dump air, N_2, and likely CO_2-laser mixtures (see [1] and references therein). The spatial period of structure is determined by the (half-)wave number *k* with the largest positive eigenvalue for the initial value of E_s (see curve *a* in Fig. 8). However, competition between current stripes has a substantial effect on their evolution, leading to suppression of one of the neighboring current stripes. The competition between them is irregular, and the pattern in Fig. 7 is one of a number of realizations.

At small current densities the period of current structures decreases with increasing *J* (see Fig. 8) in agreement with experimental results [3]. However, when the current density is more than its value at the saddle-node point, the period of current structures may increase with *J*. The period and the characteristic times of formation of the current structure and their realignment are comparable with those obtained for like conditions in experiment [4].

According to our numerical investigations, the generated structures are stable against any small perturbations. However, an attempt to change over from the large stripe with $I = 200$ mA/cm to one with $I = 100$ mA/cm by a severe decrease in the control parameter E_s leads to the formation of the three identical and equidistant stripes with the net current $I = 100$ mA/cm (see Fig. 9). It is significant that the closely spaced points (0.083 66, 0.001 594) and (0.083 68, 0.001 576) for the stripes with $I = 200$ and 100 mA/cm, respectively, are placed in the vicinity of the local minimum of curve *c* (under curve *b*) in Fig. 2(a). The point (0.083 58,

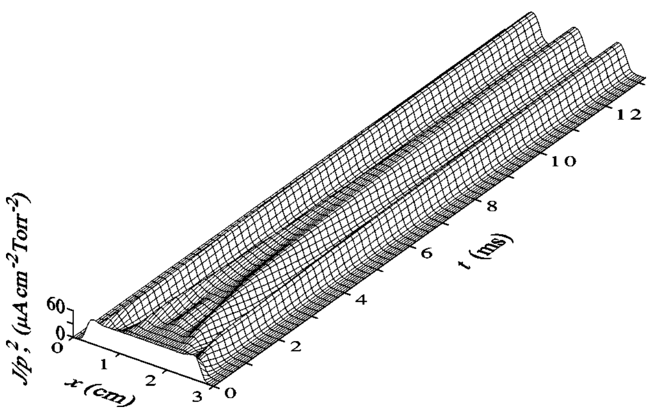

FIG. 9. Decay of the large steady current structure after severe reduction in the control parameter E_s. Parameters are $I(t=0) = 200$ mA/cm and $I(t > 0.2\text{ ms}) \simeq 100$ mA/cm. All other conditions were the same as in Fig. 5.

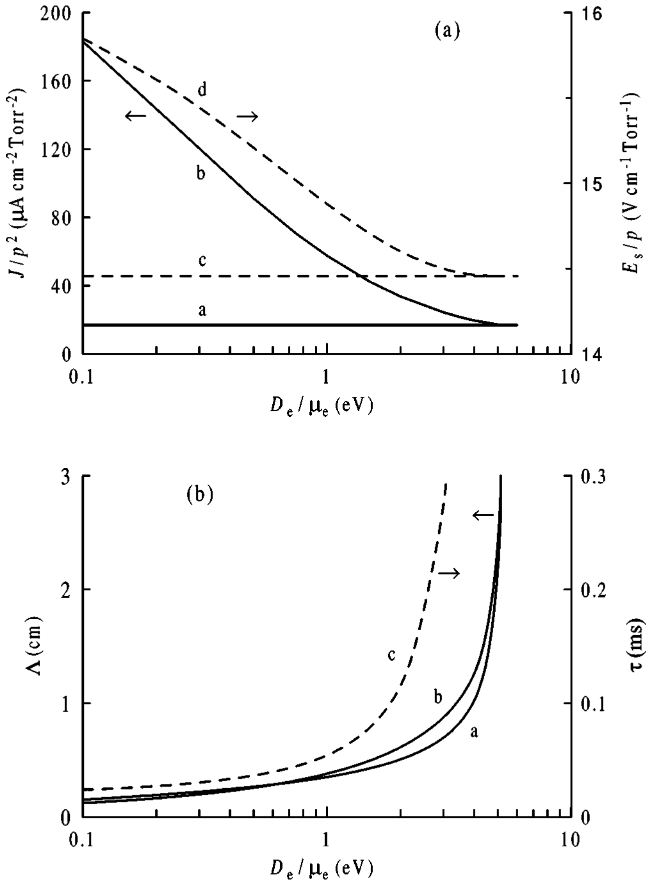

FIG. 10. (a) Dependences of the normalized current density J/p^2 and electric field E_s/p for the saddle-node point (curves *a* and *c*, respectively) and critical point of the Turing instability (curves *b* and *d*, respectively) as functions of D_e/μ_e. (b) Dependences of the transverse period Λ [defined as inverse of *q* for the maximum of the curve $\lambda(q)$] for saddle-node point (curve *a*) and critical point of the Turing instability (curve *b*) and the characteristic instability growth time τ [defined as inverse of the largest positive eigenvalue λ at the maximum of the curve $\lambda(q)$] for saddle-node point (curve *c*) as functions of D_e/μ_e (curve *b*). At $D_e/\mu_e = 1$ eV the physical parameters of the model are as in Fig. 5 and hence all parameters including the saddle-node and critical points confirms to Fig. 2.

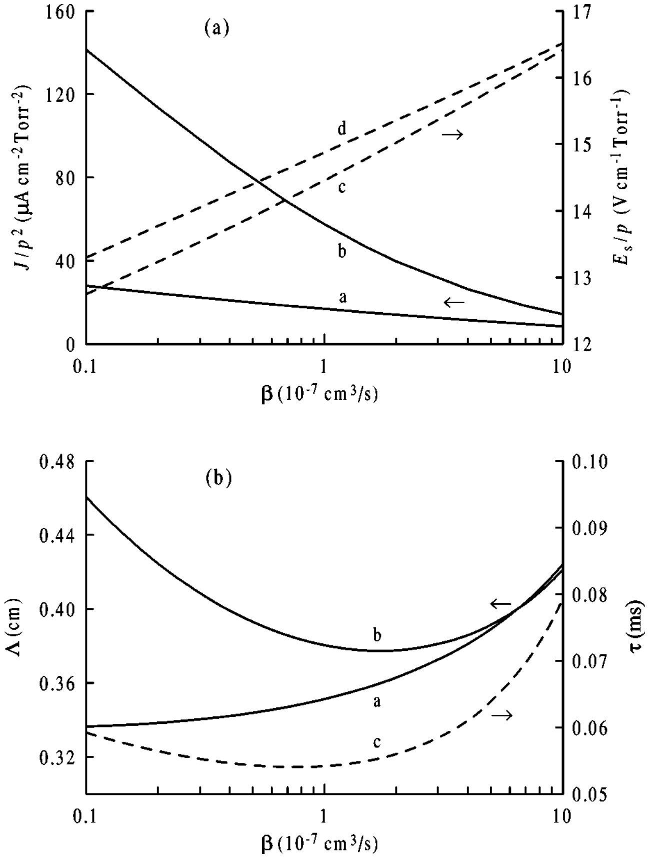

FIG. 11. Curves are the same as Fig. 10, but as functions of the electron-ion recombination coefficient β. At $\beta = 1\times10^{-7}$ cm^3/s all parameters confirms to Fig. 2.

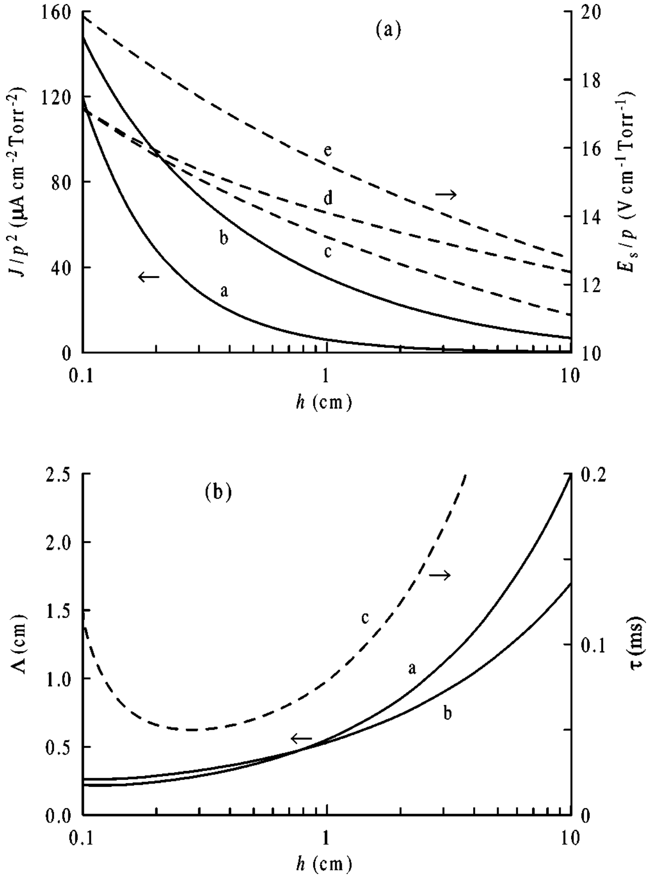

FIG. 12. Curves are the same as Fig. 10, but as functions of the discharge gap H. Additionally (a) curve e shows the normalized electric fields E_s/p for the bifurcation point with $k=0$ of the trivial solution as a function of H. At $H=0.45$ cm all parameters confirms to Fig. 2.

0.002 018) for the stripe with $I=33.3$ mA/cm is placed at the maximum of this curve. The stripes with $I>200$ mA/cm are unstable under the no-flux boundary conditions and used transverse size $L=3$ cm, and the system transfers to a stable homogeneous state lying on curve b above point C [see Fig. 2(a)]. If subsequently E_s is decreased, the system shows hysteresis.

We now consider the characteristic properties of the homogeneous and stationary solutions that describe the equilibrium states of model (23)–(25). The behavior found in the model is determined by the relative positions of saddle-node point A, the critical point of the Turing instability C, and initial homogeneous equilibrium state (say, point ×) [see Fig. 2(a)]. The influence of D_e/μ_e, β, and H on the position of points A and C in physical units and the characteristic time of instability τ and the transverse period Λ is shown in Figs. 10, 11, and 12, respectively. Saddle-node point A is independent of D_e/μ_e variations. But τ and Λ increase sharply at this point and the range $(E_*/p, E_c/p)$ of the Turing instability is diminished with D_e/μ_e (Fig. 10). In the case under consideration the contraction of transversely bounded systems is unlikely to be possible as $D_e/\mu_e > 5.3$ eV. The high magnification of the diffusion coefficients is made possible by gas flow turbulence. The saddle-node point is shifted to a position with the lower current density and higher electric field as β is increased [Fig. 11(a)]. At the same time the range of the Turing instability is diminished. The system is more stable for a large values of β. Increasing the discharge gap H shifts the saddle-node point to the lower both current density and electric field, and the period of stripes may be considerably enhanced (Fig. 12). At $H>1.9$ cm the initial equilibrium state with mean current $\overline{J}=5$ A/cm^2 discussed above [see point × in Fig. 2(a)] shifts into the Turing instability region. Additional curve e in Fig. 12(a) shows the normalized electric field E_s/p for the D_e/μ_e- and β independent instability threshold of trivial solution as a function of H. Note that there is a distinct minimum in H and β dependences of the instability growth time τ at the saddle-node point.

It is of interest to consider the properties of the model with the constraint $J=\text{const}$. Under this condition the anode potential drop U is approximately linear in the pressure p (Fig. 13) and this is in agreement with experimental observations in air [2,26]. The average electric field E_s increases with pressure at low currents (as in experiment [27]), however, the opposite situation may occur at moderate currents (Fig. 13). This behavior is dependent on the ratio between values of initial equilibrium and saddle-node point currents. The positive column, by itself, normally exhibits a negative $E_p(p)$ characteristic. At fixed J and p the anode potential

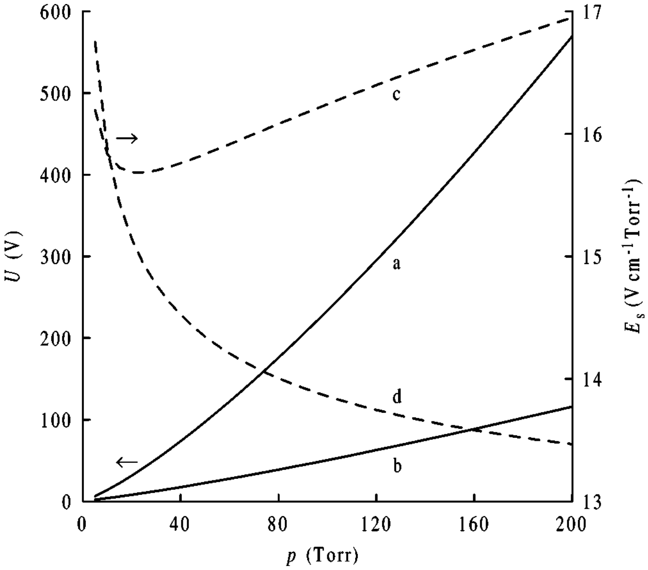

FIG. 13. Dependences of U (curves a and b) and E_s/p (curves c and d) as functions of pressure p. Current density $\overline{J}$ is 5 mA/cm^2 (curves a and c) and 50 mA/cm^2 (curves b and d). At $p=40$ Torr the physical parameters are as in Fig. 5 and hence confirms to Fig. 2.

drop U and the anode sheath thickness X_ρ are practically independent of the discharge gap H. This appears to be physically reasonable, but is inconsistent with observations in air [26]. In another experiment in air [22] the H dependence of U is not as strong as in [26]. Experimentally the case $J=$const were examined in detail, unfortunately, in air only. In an electronegative plasma refined versions of Eqs. (14) and (13) contain an additional parameter $1+n_-/n_e$ with n_- being the negative ions density [20]. If this parameter is a function of H, the anode potential drop U and the anode sheath thickness X_ρ may be depended on the discharge gap H.

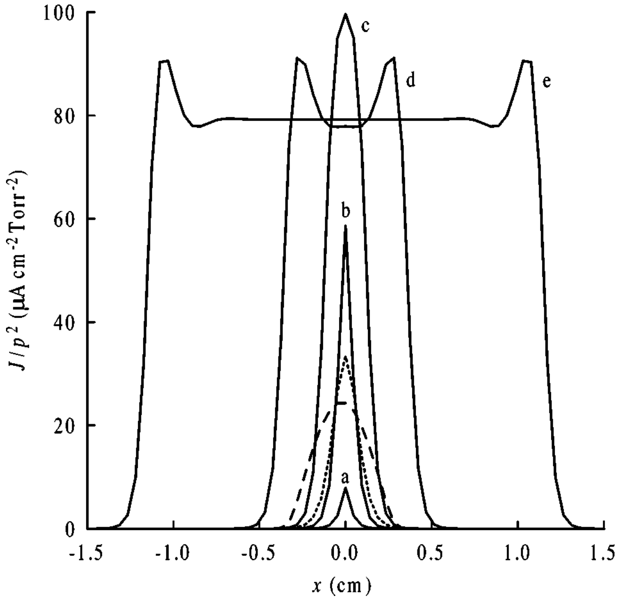

FIG. 14. Transverse profile of the normalized current density J/p^2 for various values of the net current through a stripe (curves a, b, c, d, and e for $D_e/\mu_e=1$ eV and various $I=1$,10, 40, 100, and 200 mA/cm, respectively; dashed curve for $D_e/\mu_e=2$ eV and $I=10$ mA/cm; dotted curve for $D_e/\mu_e=1$ eV and $I=15$ mA/cm from [25]). All other conditions were the same as in Fig. 5.

V. APPLICATION TO A LOCALIZED ANODE CURRENT STRUCTURE

Curve c in Fig. 2(a) describes the F_s dependence of the dimensionless averaged electron density n_0 at the middle of

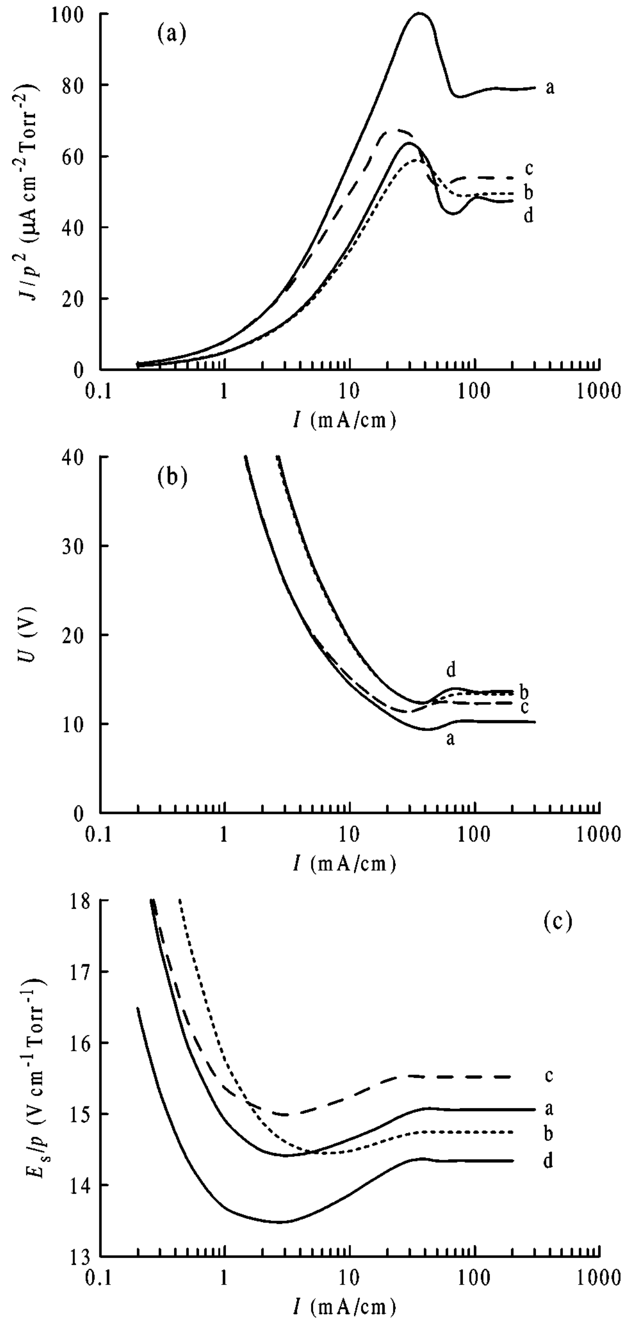

FIG. 15. Dependences of (a) J/p^2 and (b) U at the middle of a single localized stationary stripe and (c) E_s/p as functions of the net current I through a stripe. Physical parameters are as in Fig. 5 (curve a). This curve confirms to curve c in Fig. 2(a). Curves b, c, and d calculated at double D_e/μ_e, β, and H, respectively.

a single localized steady structure (stripe). The F_s dependence of the dimensionless transverse size $\mathbf{\Delta}=\int n d\widetilde{x}/n_0$ of this stripe is shown in Fig. 2(b). The current-density profiles across the discharge for the stripes are shown in Fig. 14. From this figure we notice that increasing the current through a constricted discharge causes the glowing region to just fill the anode area in accordance with the normal low current (at $I \geqslant 40$ mA/cm). The existence of a critical value of bifurcation parameter F_k such that the transverse size $\mathbf{\Delta}\rightarrow\infty$ as $F_s \rightarrow F_k$ [see Fig. 2(b)] is typical for bistable activator-inhibitor systems [24]. In the case under consideration it seems likely that this critical point $(F_k, n(F_k))$ is lying on curve *c* [see Fig. 2(a)] and thence the normal current density and normal anode voltage drop are a point of the homogeneous equilibrium state of the model. Earlier the normal current effect in the near-anode region has been investigated in the frame of the basic model (1) and (2) in cylindrically symmetric geometry [28]. The shape of the subnormal spot is governed by located ionization processes and diffusion charge particles, while the normal anode spot is formed under the influence of the ionization and recombination processes and the transverse transport of charge particles in complicated electric field. When D_e/μ_e increases (dashed curve in Fig. 14), the current profile becomes more spread. A comparison of the calculated results with [4] revealed that the current-density profile of the basic model is smoother and wider than that from model (23) and (24) (see Fig. 14).

Figure 15 shows the dependences of J/p^2 and U at the middle of stripe and E_s/p as functions of the net current I through the stripe. Curve *a* corresponds the data for $D_e/\mu_e = 1$ eV in Fig. 14. Figure 15(a) shows that in the intermediate range of current (say, $3 < I < 20$ mA/cm) the current density increases logarithmically with an increase in the discharge current. The subnormal stripes with very low currents are independent of recombination processes and would require an increased electric field and a great anode voltage drop (Fig. 15). The normal current density decreases with D_e/μ_e [see curves *a* and *b* in Fig. 15(a)]. It seems likely that this effect is even more pronounced than in the case of cylindrically symmetric geometry [28]. The stripe parameters $(J/p^2, U)$ are defined by rather a summary diffusion loss $(\sim HD_e)$ [see curves *b* and *d* in Figs. 15(a) and 15(b)]. However the D_e/μ_e- and H dependences of the average electric field E_s are essentially different.

VI. CONCLUSION

We presented a one-dimensional physically self-consistent model of high-pressure dc discharges that takes into account the main physical processes in near-anode plasma and positive column. The model involves a pair of coupled reaction-diffusion equations of an activator-inhibitor-type. Numerical simulations show that this model displays spontaneous generation of complex current structures or a single spot at the anode and reflects most of the properties of basic multidimensional drift-diffusion model (1) and (2). In contrast to the variables of basic equations (1) and (2), the variables of model (23) and (25) admit homogeneous solutions in the strongly longitudinal-inhomogeneous near-anode layer. This makes possible the using of standard stability and bifurcation analysis. The discharge gap, volume electron-ion recombination, and especially electron diffusion have a profound effect on the collective interaction of current structures. The predictions of the model match the available experimental results to a satisfactory extent, particularly with respect to the anode pattern formation.

---

[1] V. S. Golubev and S. V. Pashkin, *Tleyushchii Razryad Povyshennogo Davleniya* (*Elevated-Pressure Glow Discharge*) (Nauka, Moscow, 1990).

[2] R. I. Kopyrina, G. D. Mylnikov, and A. A. Vedenov, in *Proceedings of the XIIth International Conference on Phenomena in Ionized Gases, Eindhoven, 1975,* edited by J. G. A. Holscher and D. C. Schram (North-Holland, Amsterdam, 1975), p. 58.

[3] Yu. S. Akishev, A. M. Volcheck, A. P. Napartovich, and N. I. Trushkin, Plasma Sources Sci. Technol. **1**, 190 (1992).

[4] R. Sh. Islamov, O. A. Novodvorskii, and R. Ya. Sagdeev, Fiz. Plazmy **23**, 970 (1997) [Plasma Phys. Rep. **23**, 895 (1997)].

[5] W. Breazeal, K. M. Flynn, and E. G. Gwinn, Phys. Rev. E **52**, 1503 (1995).

[6] E. Ammelt, Yu. A. Astrov, and H.-G. Purwins, Phys. Rev. E **55**, 6731 (1997).

[7] A. M. Dykhne and A. P. Napartovich, Dokl. Akad. Nauk SSSR **247**, 837 (1979) [Sov. Phys. Dokl. **24**, 632 (1979)].

[8] G. G. Gladush and A. A. Samokhin, Fiz. Plazmy **11**, 230 (1985) [Sov. J. Plasma Phys. **11**, 136 (1985)].

[9] I. Müller, C. Punset, E. Ammelt, H.-G. Purwins, and J. P. Boeuf, IEEE Trans. Plasma Sci. **PS-27**, 20 (1999).

[10] R. Sh. Islamov, in *Contributed Papers of the IIIrd International Conference on Plasma Physics and Plasma Technologies, Minsk, Belarus, 2000* (Institute of Molecular and Atomic Physics NAS of Belarus, Minsk, 2000), Vol. 1, p. 19.

[11] R. Sh. Islamov, Izv. Ross. Akad. Nauk, Ser. Fiz. **64**, 1402 (2000) [Bull. Russ. Acad. Sci. Physics **64**, 1126 (2000)].

[12] C. Radehaus, T. Dirksmeyer, H. Willebrand, and H.-G. Purwins, Phys. Lett. A **125**, 92 (1987).

[13] K. G. Müller, Phys. Rev. A **37**, 4836 (1988).

[14] K. Krischer and A. Mikhailov, Phys. Rev. Lett. **73**, 3165 (1994).

[15] Yu. A. Astrov and Yu. A. Logvin, Phys. Rev. Lett. **79**, 2983 (1997).

[16] C. Radehaus, R. Dohmen, H. Willebrand, and F.-J. Niedernostheide, Phys. Rev. A **42**, 7426 (1990).

[17] M. S. Benilov, Phys. Rev. A **45**, 5901 (1992).

[18] K. G. Emeleus, Int. J. Electron. **52**, 407 (1982).

[19] R. Sh. Islamov, Izv. RAN, Mekh. Zhidk. i Gaza **2**, 172 (1994) [Fluid Dyn. **29**, 291 (1994)].

[20] R. Sh. Islamov, J. Appl. Phys. **79**, 8253 (1996).

[21] Y. L. Luke, *Special Functions and Their Approximations* (Academic, New York, 1969).

[22] V. I. Blokhin, V. V. Breev, S. V. Dvurechenskii, and S. V.

Pashkin, Teplofiz. Vys. Temp. **19**, 897 (1981) [High Temp. **19**, 647 (1981)].

[23] N. G. Chetaev, *Stability of Motion* (Pergamon Press, New York, 1961).

[24] B. S. Kerner and V. V. Osipov, *Autosolitons* (Kluwer, Dordrecht, 1994).

[25] R. Sh. Islamov, IEEE Trans. Plasma Sci. **PS-27**, 88 (1999).

[26] V. I. Blokhin and S. V. Pashkin, Teplofiz. Vys. Temp. **14**, 378 (1976) [High Temp. **14**, 337 (1976)].

[27] E. P. Velikhov, V. S. Golubev, and S. V. Pashkin, Usp. Fiz. Nauk **137**, 117 (1982) [Sov. Phys. Usp. **25**, 340 (1982)].

[28] R. Sh. Islamov and E. N. Gulamov, IEEE Trans. Plasma Sci. **PS-26**, 7 (1998).